

Neural Fields with Thermal Activations for Arbitrary-Scale Super-Resolution

Alexander Becker^{1,*} Rodrigo Caye Daudt^{1,*} Nando Metzger¹
 Jan Dirk Wegner² Konrad Schindler¹
¹ETH Zurich ²University of Zurich

Abstract

Recent approaches for arbitrary-scale single image super-resolution (ASSR) have used local neural fields to represent continuous signals that can be sampled at different rates. However, in such formulation, the pointwise query of field values does not naturally match the point spread function (PSF) of a given pixel. In this work we present a novel way to design neural fields such that points can be queried with a Gaussian PSF, which serves as anti-aliasing when moving across resolutions for ASSR. We achieve this using a novel activation function derived from Fourier theory and the heat equation. This comes at no additional cost: querying a point with a Gaussian PSF in our framework does not affect computational cost, unlike filtering in the image domain. Coupled with a hypernetwork, our method not only provides theoretically guaranteed anti-aliasing, but also sets a new bar for ASSR while also being more parameter-efficient than previous methods.

1. Introduction

For years, learning-based image super-resolution (SR) methods have achieved ever better results. But unlike interpolation methods, which allow us to resample a given image at any resolution, such methods require retraining for each desired scaling factor. In recent years, several supervised methods for arbitrary-scale SR (ASSR) have been proposed to allow end-users to choose any scaling factor, rendering such systems much more flexible [17]. Notably, Chen et al. [11] pioneered the use of neural fields for single-image super-resolution (SR) with LIIF, exploiting the continuous representation to enable SR at arbitrary scaling factors. Their method has inspired several follow-ups which build upon the idea of using local neural fields [8, 10, 22]. This is not surprising: Neural fields are in many ways a natural match for variable-resolution computer vision and graphics [43]. By implicitly parameterizing a target signal as a neural network that maps coordinates to signal strength,

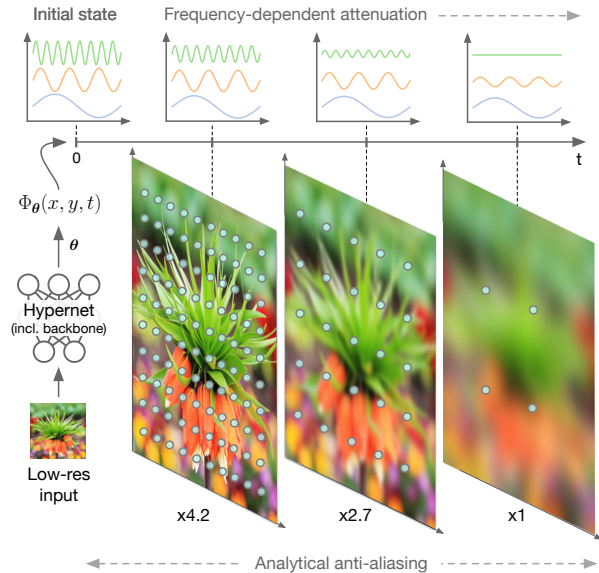


Figure 1. Given a low-resolution input, a hypernetwork predicts the parameters of a customized neural field $\Phi_\theta(x, y, t)$ composed of sinusoidal components. We obtain Gaussian-filtered (anti-aliased) versions of the image that correspond to arbitrary pixel sizes by simply modulating the components according to their frequencies. This representation can then be queried at arbitrary coordinates (x, y, t) to recover pixel grids at any desired scaling factor.

they offer a compact representation, defined over a continuous input domain, and analytically differentiable. Among others, they have been widely adopted for 3D reconstruction with radiance [30], occupancy [29, 35], and distance fields [33, 37].

Neural fields offer a compelling representation of continuous signals. However, for many tasks it is not desirable to query such fields at a single point, but rather to have an integral observation model such as a point spread function (PSF) [3]. This is not trivial [3–5, 16]. For ASSR, where the signal should be observed at various scales and is prone to aliasing, a neighborhood-dependent observation model is desirable. Using appropriate observation modeling has not only the potential to reduce aliasing but also to more ac-

*Equal contribution. Contact: alexander.becker@geod.baug.ethz.ch

curately reflect the physical processes of image acquisition. For this reason, Chen et al. [11] already took a first step towards learning multiscale representations through cell encoding. For radiance fields, Mip-NeRF [3] and subsequent work [4, 5, 16] have explored ways to mitigate aliasing effects by focusing on the positional encoding of the location \mathbf{x} as a tool to control different frequencies in Φ .

In our work, we combine recent advances in implicit neural representations with ideas from classical signal theory to develop a neural field that *guarantees anti-aliasing by construction*. Furthermore, this filtering incurs no additional overhead: The cost of querying a field’s value does not depend on the size of the anti-aliasing filter. The key insight is that when using sinusoidal activation functions [38], one can decay different components at different rates based on their frequencies, according to Fourier theory. Inspired by the connection between Fourier decompositions and the heat equation, we propose Thera, an ASSR method with neural fields that uses a novel thermal activation function (see Fig. 1). This formulation makes it possible to analytically compute Gaussian-blurred versions of a field $\Phi(\mathbf{x})$ for any desired (isotropic) blur radius. This is equivalent to querying Φ with a Gaussian PSF. Thera outperforms competing methods in most of our experiments, is far more parameter-efficient, and provides theoretical guarantees w.r.t. anti-aliasing and multi-scale representation. We demonstrate that a lightweight variant of our algorithm still outperforms most previous methods while using 2-4 orders of magnitude fewer parameters. To provide theoretical guarantees for our thermal activations, certain constraints are imposed on the field’s neural architecture. Fortunately, these constraints can easily be overcome with the help of a hypernetwork [14], so that our method can seamlessly integrate a wide range of well-proven SR backbones. In summary, our main contributions are:

1. We introduce thermal activations, which enable neural fields with a principled Gaussian observation model, and as a consequence anti-aliasing with minimal overhead.
2. We use thermal activations to build Thera, a novel method for ASSR which is superior to previous methods while being more parameter efficient and providing theoretical guarantees w.r.t. multiscale representation.

2. Related work

Arbitrary-scale SR. In recent years, research on arbitrary-scale super-resolution (ASSR) methods has gained attention. In ASSR the scaling factor can be chosen at inference time to be any positive number, which allows for maximum flexibility, such as that of interpolation methods. The first work along this line is MetaSR [17], which infers the parameters of a convolutional upsampling layer using a hypernetwork, conditioned on the desired scaling factor. An influential successor work is LIIF [11], in which the high-

resolution image is implicitly described by a neural field that is locally conditioned with features extracted from the low-resolution image. The continuous nature of the neural field allows for sampling target pixels at arbitrary locations, and thus also arbitrary resolution. Following work has since built upon the LIIF framework. For instance, UltraSR [45] improves modeling of high-frequency textures with periodic positional encodings of the coordinate space, as is common practice for neural radiance fields. LTE [22] makes learning higher frequencies more explicit by effectively implementing a learnable coordinate transformation into 2D Fourier space, prior to a forward pass through an MLP. Vasconcelos et al. [41] use neural fields in CUF to parameterize continuous upsampling filters, which enables arbitrary-scale upsampling. Most recently, methods have integrated attention mechanisms into their implicit representation, enabling the neural field to adaptively attend to image features depending on the query coordinates and scale factor, improving reconstruction quality [8, 10]. These methods provide the required scaling factor explicitly as an input to the field, thus attempting to learn the observation model from data. In this paper, we explore a way to directly integrate such a model into the neural field representation.

Implicit neural representations. A neural field is a neural network trained to map real-valued coordinates onto a field’s values. Recently, neural fields have been used for parameterizing various types of visual data, including images [11, 12, 20, 22, 38, 39], 3D scenes (e.g., represented as signed distance fields [33, 37, 38, 42], occupancy fields [29, 35], LiDAR fields [19], view-dependent radiance fields [3–5, 30]), or digital humans [9, 13, 44, 46, 49]. We refer the interested reader to Xie et al. [43] for a comprehensive survey of neural fields in vision and beyond. Frequently, it is desirable to impose some prior over the space of learnable representations. A common approach for such conditioning of neural fields is encoder-based inference [43], where a parametric encoder maps input observations to a set of latent codes \mathbf{z} , which are often local [8, 10, 11, 22, 41]. The encoded latent variables \mathbf{z} are then used to condition field parameters θ , for instance by simply concatenating \mathbf{z} to the coordinate inputs or through a more expressive *hypernetwork* [14]. The latter is a trainable neural network $\Psi: \mathbf{z} \mapsto \theta$, mapping latent codes to field parameters. An early example of this is Sitzmann et al. [38], and this approach is gaining popularity [43].

Anti-aliasing in neural fields. Early in the recent development of implicit neural representations, concerns regarding aliasing were raised. Barron et al. [3] proposed integrating the positional encoding with Gaussian weights, which reduced aliasing in NeRF. Improvements were later proposed for unbounded scenes [4] and to improve efficiency [16]. Barron et al. [5] tackle anti-aliasing for the increasingly popular Instant-NGP [31] approach. In ASSR, methods

usually provide the desired scale as input and expect to learn it from data [8, 11].

3. Method

To understand how anti-aliasing can be computed analytically, we must first define a sampling model and recap a well-established result from Fourier analysis. While we stick to the 2D case here for simplicity, all theory is valid for signals with any number of dimensions. We refer the reader to [32] for an in-depth analysis of sampling and aliasing.

To minimize aliasing when sampling a continuous signal $f(\mathbf{x})$ in 2D image space, $\mathbf{x} \in \mathbb{R}^2$, it is necessary to suppress high-frequency parts of the signal that cannot be represented at the desired sampling rate. One must apply a low-pass filter $g(\mathbf{x})$ whose cut-off frequency is aligned with the Nyquist frequency of the sampling rate, and then sample the band-limited signal $f \otimes g(\mathbf{x})$. Here, we show that one can naturally integrate this behavior into a neural field’s architecture. The key to this is knowing that if a signal is decomposed into sinusoidal components, filtering can be done simply by *re-scaling each component by a frequency-dependent factor*. This equivalence is depicted in Fig. 2. While decomposing a given signal into sinusoidal components is normally a costly operation, we show that we can avoid it by designing a neural field in which *the decomposition itself is the native representation of the signal*.

3.1. Thermal activation functions

The intuition behind our method goes back to the starting point of Fourier analysis: the heat equation. Other implicit representation methods, such as SIREN [38], optimize the parameters θ_Φ of a field $\Phi(\mathbf{x})$ by minimizing a data fidelity term $\mathbb{E}_{(\mathbf{x}_i, \mathbf{y}_i \sim \mathcal{D})} [\mathcal{L}(\Phi(\mathbf{x}_i), \mathbf{y}_i)]$ over a dataset \mathcal{D} . Our key insight is the following: What if we take this field to represent the temperature distribution on a surface at a given time t_0 ? It is well known how to solve the heat equation forwards in time – its solution (on an isotropic surface) is given by a Gaussian blur of the state at t_0 , where the blur radius depends on the time difference $t - t_0$. Our field $\Phi(\mathbf{x}, t)$ now has an additional temporal dimension, but given a single slice $\Phi(\mathbf{x}, t_0)$ there is a unique solution $\Phi(\mathbf{x}, t)$ for every $t \geq t_0$ such that the field obeys the heat equation

$$\frac{\partial \Phi}{\partial t} = \kappa \cdot \nabla_{\mathbf{x}}^2 \Phi = \kappa \cdot \left(\frac{\partial^2 \Phi}{\partial x_1^2} + \frac{\partial^2 \Phi}{\partial x_2^2} \right), \quad (1)$$

where $\kappa > 0$ is the thermal diffusivity of the medium. The solution for $0 \leq t < t_0$ is, however, ill-posed, mirroring the fact that image downsampling is well-posed, but super-resolution is not.

A naive attempt to ensure that Φ respects the heat equation in Eq. (1) would be to include an additional loss term: $\left| \frac{\partial \Phi}{\partial t} - \kappa \cdot \nabla_{\mathbf{x}}^2 \Phi \right|$. Despite our best efforts, this approach

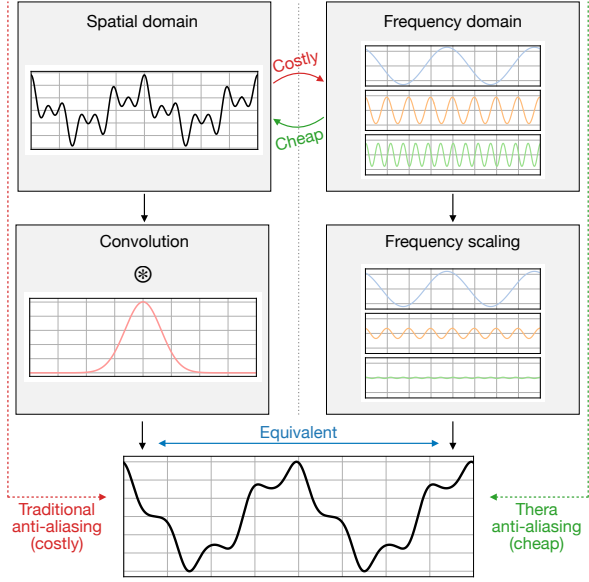


Figure 2. If we have access to the sinusoidal decomposition of a signal, filtering can be done analytically by scaling each component appropriately. We design our neural field so that we have access to such a decomposition at no extra cost.

was unsuccessful. Nevertheless, it turns out that we can design the field’s architecture in such a way that it is *guaranteed* to respect Eq. (1). We do so by formulating Φ as a two-layer perceptron

$$\mathbf{y} = \mathbf{W}_2 \cdot \xi(\mathbf{W}_1 \mathbf{x} + \mathbf{b}_1, \nu(\mathbf{W}_1), \kappa, t) + \mathbf{b}_2, \quad (2)$$

where ν refers to the wave numbers (frequencies) implied by \mathbf{W}_1 , described in more detail later; and the thermal activation function $\xi(\cdot)$ models the decay of different sinusoidal components over time. We set $t = 0$ to be the (unobservable) initial thermal state of a given system represented as a sum of sinusoidal components:

$$\xi(\mathbf{z}, \nu, \kappa, 0) = \sin(\mathbf{z}). \quad (3)$$

For $t > 0$, each component is decayed according to its wave number, the thermal diffusivity constant κ , and t :

$$\xi(\mathbf{z}, \nu, \kappa, t) = \sin(\mathbf{z}) \cdot \exp(-|\nu|^2 \kappa t). \quad (4)$$

To obtain $|\nu(\mathbf{W}_1)|$ we can simply compute the row-wise Euclidean norm of \mathbf{W}_1 , corresponding to the magnitudes of the implied wave numbers (direction is irrelevant, as all components with the same frequency decay equally over time, regardless of their orientation). Equation (4) results in higher-frequency components decaying faster than lower-frequency ones, giving rise to a Gaussian low-pass filter whose strength increases with time t .

There is an ideal bijection between the sampling rate f_s and t . At $t = 0$ no filtering takes place, implying a continuous signal ($f_s \rightarrow \infty$). A low-pass filtered version of the

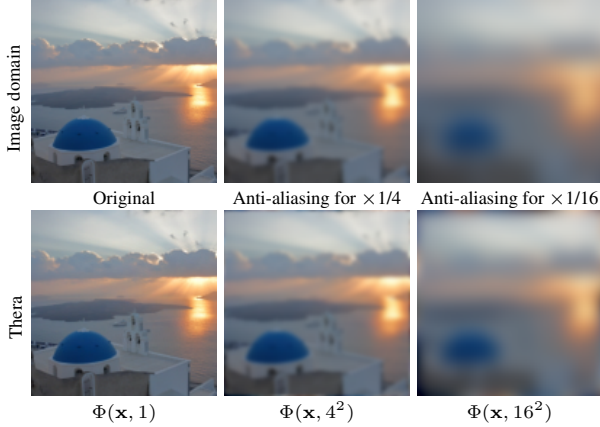


Figure 3. Comparison between a theoretical anti-aliasing filter and Thera’s anti-aliasing, which is computed without convolutions or over-sampling. Note that the field was only supervised at $\Phi(\mathbf{x}, 1)$.

signal is observed for $t > 0$. To obtain a desired level of anti-aliasing, we only need to compute the corresponding value of t . The relationship between the cut-off frequency of the filter and t is controlled by κ , which we can freely set to any positive number. For simplicity, and without loss of generality, we set κ such that the native resolution of the (observed, discrete) signal \mathcal{D} is $t = 1$. Assuming equal sampling rate f_s along both coordinate axes, the optimal value of κ then evaluates to

$$\kappa = \frac{\sqrt{\log(4)}}{2f_s\pi^2}. \quad (5)$$

To subsample the signal \mathcal{D} by a factor S , Φ should be sampled at

$$t = S^2. \quad (6)$$

The derivations of these values can be found in Appendix A.

In our formulation, \mathbf{W}_1 can be seen as a frequency bank whose components (“basis functions”) make up the signal $\Phi(\mathbf{x}, 0)$, and the vector \mathbf{b}_1 represents the phase shifts of those components. The matrix \mathbf{W}_2 , with one row per output channel, contains the initial ($t = 0$) magnitudes of these components, and \mathbf{b}_2 is the global bias of Φ per channel.

Figure 3 shows an example where we fit the signal at $t = 1$ to the image. After training, any low-pass filtered version of the image can be generated by setting t according to Eq. (6). We emphasize that: (i) Computing these filtered images requires no over-sampling or convolutions; (ii) The computational cost does **not** depend on the size of the blur kernel or on t ; (iii) Given $\Phi(\mathbf{x}, t_0)$, $\Phi(\mathbf{x}, t)$ is known for any $t \geq t_0$.

By definition, such field Φ follows the heat equation and is therefore able to perform anti-aliasing at arbitrary sampling frequencies. An alternative (equivalent) interpretation is to view $\Phi(\mathbf{x}, t)$ as an observation of the true, continuous

signal $\Phi(\mathbf{x}, 0)$ with a Gaussian point spread function whose width (standard deviation) is determined by t .

3.2. Thermal activations for super-resolution

The multi-scale signal representation defined above is a natural match for super-resolution, and particularly well-suited if arbitrary scale factors shall be covered. Still, two challenges must be addressed. First, our formulation restricts the choice of architecture. Second, while it theoretically guarantees the downsampling operation ($t > t_0$), the up-sampling operation ($0 < t < t_0$) remains ill-posed. To narrow down the (infinite) solution space to a unique result a prior must either be defined in an unsupervised fashion or learned from data. We describe below how these issues can be addressed, so that Thera can be used to model local fields that represent each pixel in the low-resolution image, a strategy initially proposed by LIIF [11] and used by most recent ASSR methods [8, 10, 22, 41].

Our solution to both challenges is to condition local fields with a hypernetwork $\Psi : \mathbb{R}^{W \times H \times 3} \rightarrow \mathbb{R}^{W \times H \times N}$, where N is the number of parameters in a field of the desired size. Given a low-resolution image, the hypernetwork maps it to parameters for local fields, each spanning the area of one pixel of the low-resolution input. Even though the fields themselves model only a local part of the image, the hypernetwork informs them with rich contextual features collected over a large receptive field. The hypernetwork Ψ is composed of a standard SR backbone, as used in previous work [8, 10, 11, 22, 41], followed by one or more layers which produce feature maps of depth N . In this work, we use a series of ConvNeXt [25] blocks for this purpose. The local fields themselves are then supervised with values from high-resolution target pixels at the appropriate spatial coordinates \mathbf{x} and temporal coordinate t . The latter ensures that the signal has been filtered to the correct target resolution prior to querying discrete pixel values. Similar to LIIF, we use a local coordinate system for every field that is bounded in $[-0.5, 0.5] \times [-0.5, 0.5]$. The components \mathbf{W}_1 are optimized directly rather than being an output of Ψ . Not only does this better fit the idea of having a consistent basis with which we represent each signal, but it also reduces the number of total parameters and, as we show later, leads to better results.

The described scheme, Thera, is depicted in Fig. 4. It allows for arbitrary-scale super-resolution combining the power of proven feature extractors for SR and image restoration with the presented multiscale representation capabilities. As the entire network is trained end-to-end, the feature extractor can learn super-resolution priors from data that lie within the resolution range observed during training. *E.g.*, a network trained with scaling factors up to $\times 4$ will encode priors that enable us to observe the field at $\frac{1}{16} < t$. By training using multiple resolutions, we can also make κ a

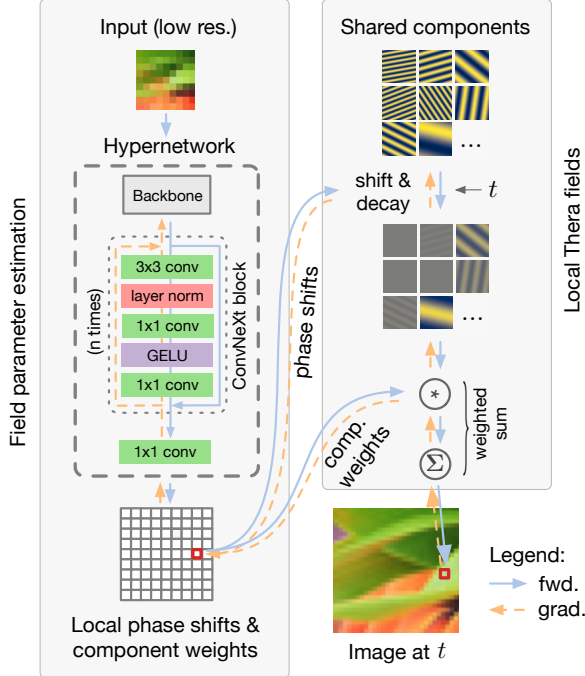


Figure 4. Overview of Thera. A hypernetwork estimates the parameter of local fields. Each field uses thermal activations for multi-scale signal representation and anti-aliasing.

trainable parameter to allow the network to adapt to different downsampling operators. We also manually set the bias of each channel of Φ to the RGB values of its associated low-resolution pixel.

Priors at $t = 0$. To perform ASSR for out-of-domain scaling factors, we can use unsupervised priors at $t = 0$. Note that this is a prior *on the continuous signal itself* – something that, to the best of our knowledge, sets Thera apart from all previous methods. In our implementation, that prior takes the form of a total variation (TV) loss term, well known to promote piece-wise constant signals that describe natural images well. We use an ℓ^1 variant of TV:

$$\mathcal{L}_{\text{TV}}(\Phi(\mathbf{x}, 0)) = \mathbb{E}_{\mathbf{x}}[|\nabla\Phi(\mathbf{x}, 0)|]. \quad (7)$$

Given our continuous signal representation, $\nabla\Phi(\mathbf{x}, 0)$ can be computed *analytically* using automatic differentiation tools, rather than using a neighborhood approximation as done most often in previous work [36].

Implementation and training. We use JAX [7] to implement Thera to maximize the efficiency of the hypernetwork operations. A PyTorch [34] implementation to fit a Thera field to a single image is also provided. Similar to prior work [11, 22], we randomly sample a scaling factor $r \sim \mathcal{U}(1.2, 4)$ for each image during training, then randomly crop an area of size $(48r)^2$ pixels as the target patch, from which the source is generated by bicubic downsampling to a patch of size 48^2 . As corresponding targets,

48^2 random pixels are sampled from the target patch. We train with the Adam optimizer [21] with an initial learning rate of 10^{-4} , $\beta_1 = 0.9$, $\beta_2 = 0.999$ and $\epsilon = 10^{-8}$ for 5×10^6 iterations with a batch size of 16. Throughout the optimization, the learning rate is decayed to zero according to a cosine annealing schedule [26]. We use a mean absolute error (MAE) loss for training, to which the TV loss from Eq. (7) is added with a weight of 10^{-4} . Standard data augmentations are used during training, including random flipping, rotations, and resizing of images. Analogous to previous work [24, 40, 41], we implement geometric self-ensembling, where the results of four rotated versions of the input are averaged at test time. We did not observe an improvement in performance if flips were included. Our code and pre-trained checkpoints will be made publicly available.

4. Results

We evaluate the performance of Thera on a variety of datasets and with three popular feature extractors as backbones. We also conduct an ablation study that supports the design choices described in Sec. 3. Throughout this section, we will evaluate three variants of our method which differ solely in size of the hypernetwork and field:

- Thera-S: We set the number of shared components to 32, and omit all but one layer of the hypernetwork, the layer that maps features to field parameters. This version adds only 8,256 parameters on top of the backbone.
- Thera-M: This version uses 512 shared components and a moderately sized hypernetwork (5 ConvNeXt layers), approximately matching the parameter count of medium-sized competing methods (MetaSR [17], LIIF [11], LTE [22] and CUF [41]). This amounts to 0.48 M additional parameters.
- Thera-L: We use 512 components and a larger hypernetwork (16 ConvNeXt layers), amounting to 1.41 M additional parameters. This version is comparable to CiaoSR [8] in terms of parameter count.

Datasets and metrics. Like previous methods, our models are trained with the DIV2K [1] training set, which is composed of 800 high-resolution RGB images of diverse scenes. We report evaluation metrics on the official DIV2K validation split (100 images) as well as on a set of standard benchmark datasets: Set5 [6], Set14 [47], BSDS100 [27] (all three containing natural images of low to medium resolution), Urban100 [18] (high-resolution urban scenes), and Manga109 [28] (high-resolution Japanese manga illustrations). Following prior work, we use peak-signal-to-noise ratio (PSNR, in decibels) as the evaluation metric, where PSNR is computed in RGB space for DIV2K and on the luminance (Y) channel of the YCbCr representation for benchmark datasets. Not all numbers could be computed for competing methods due to the lack of availability of code or

Backbone (params.)	Method	Num. of add. params.	In-distribution			Out-of-distribution				
			$\times 2$	$\times 3$	$\times 4$	$\times 6$	$\times 12$	$\times 18$	$\times 24$	$\times 30$
	Bicubic	—	31.01	28.22	26.66	24.82	22.27	21.00	20.19	19.59
EDSR- baseline [24] (1.22 M)	MetaSR [17]	0.45 M	34.64	30.93	28.92	26.61	23.55	22.03	21.06	20.37
	LIIF [11]	0.35 M	34.67	30.96	29.00	26.75	23.71	22.17	21.18	20.48
	LTE [22]	0.49 M	34.72	31.02	29.04	26.81	23.78	22.23	21.24	20.53
	CUF [41]	0.30 M	34.79	31.07	29.09	26.82	23.78	22.24	—	—
	CiaoSR [8]	1.43 M	34.88	31.12	29.19	26.92	23.85	22.30	21.29	20.44
	CLIT [10]	15.7 M	34.81	31.12	29.15	26.92	23.83	22.29	21.26	20.53
	Thera-S	.008 M	34.75	31.09	29.10	26.84	23.80	22.26	21.26	20.56
	Thera-M	0.48 M	34.86	31.21	29.22	26.94	23.87	22.32	21.31	20.60
Thera-L	1.41 M	34.88	31.22	29.24	26.96	23.89	22.33	21.32	20.61	
RDN [48] (22.0 M)	MetaSR [17]	0.45 M	35.00	31.27	29.25	26.88	23.73	22.18	21.17	20.47
	LIIF [11]	0.35 M	34.99	31.26	29.27	26.99	23.89	22.34	21.31	20.59
	LTE [22]	0.49 M	35.04	31.32	29.33	27.04	23.95	22.40	21.36	20.64
	CUF [41]	0.30 M	<u>35.11</u>	31.39	29.39	27.09	23.99	22.42	—	—
	CiaoSR [8]	1.43 M	35.13	31.39	<u>29.43</u>	27.13	24.03	22.45	21.41	20.55
	CLIT [10]	15.7 M	35.10	31.39	<u>29.39</u>	27.12	24.01	22.45	21.38	20.64
	Thera-S	.008 M	35.06	31.42	<u>29.43</u>	27.13	24.04	<u>22.48</u>	<u>21.44</u>	<u>20.71</u>
	Thera-M	0.48 M	34.97	31.39	<u>29.43</u>	27.15	24.05	22.49	21.44	<u>20.71</u>
Thera-L	1.41 M	34.98	31.40	29.45	27.16	24.06	22.49	21.45	20.72	
SwinIR [23] (12.0 M)	MetaSR [17]	0.45 M	35.15	31.40	29.33	26.94	23.80	22.26	21.26	20.54
	LIIF [11]	0.35 M	35.17	31.46	29.46	27.15	24.02	22.43	21.40	20.67
	LTE [22]	0.49 M	35.24	31.50	29.51	27.20	24.09	22.50	21.47	20.73
	CUF [41]	0.30 M	35.31	31.56	29.56	27.23	24.10	22.52	—	—
	CiaoSR [8]	1.43 M	35.28	31.53	29.56	27.26	24.12	22.52	21.48	20.59
	CLIT [10]	15.7 M	<u>35.29</u>	31.55	29.55	27.26	24.11	22.51	21.45	20.70
	Thera-S	.008 M	35.27	31.57	29.58	27.25	24.13	22.55	<u>21.52</u>	<u>20.77</u>
	Thera-M	0.48 M	<u>35.29</u>	31.58	<u>29.59</u>	<u>27.27</u>	24.15	<u>22.56</u>	<u>21.52</u>	<u>20.77</u>
Thera-L	1.41 M	<u>35.29</u>	31.59	29.61	27.30	24.17	22.59	21.54	20.79	

Table 1. Quantitative comparison of peak signal-to-noise ratio (PSNR, in dB) obtained by various methods on the DIV2K validation set. The highest PSNR value per backbone and scaling factor is in **bold** and the second highest is underlined.

checkpoints, see Appendix E. Additional quantitative metrics are also provided in the supplementary material.

Backbones. Following related work, we train our method jointly with three standard backbone feature extractors for super-resolution and image restoration: (i) EDSR-baseline [24] (1.22 M parameters); (ii) RDN [48] (22.0 M parameters); and (iii) SwinIR [23] (12.0 M parameters).

4.1. Super-resolution performance

We begin with evaluating the three variants of our method (Thera-S, -M, and -L) on the hold-out DIV2K validation set, following the setup described above. Table 1 shows the PSNR values obtained by all investigated methods, for both in-distribution ($\times 2$ - $\times 4$) and out-of-distribution ($\times 6$ - $\times 30$) scaling factors. Thera achieves state-of-the-art performance. Thera-L outperforms all previous methods on 22 out of 24 cases, often by a considerable margin (e.g., $\times 3$ using EDSR-baseline). Thera-M, which requires only a third as many additional parameters, still outperforms or – less frequently – is on par with competitors that have comparable parameter count in most cases. Notably, except for $\times 2$, Thera-M also matches the performance of more expensive, attention-based methods CiaoSR and CLIT, despite a more than $30\times$ fewer parameters than CLIT.

Notably, our minimal version Thera-S – enabling arbitrary-scale SR with theoretical guarantees using only 8,192 additional parameters – regularly outperforms all comparison methods except for the most parameter-intensive ones when using the EDSR backbone. Using the more powerful SwinIR backbone, Thera-S outperforms **all** previous methods (including attention-based ones) on 6 of 8 scaling factors, despite adding almost $2000\times$ fewer learnable parameters than CLIT (and $170\times$ fewer than CiaoSR) on top of the feature extractor. Similarly, with RDN our smallest variant performs best in 7 of 8 scaling factors. This confirms that having formal modeling of multi-scale representation baked into our network is highly beneficial, especially for higher scaling factors.

We further report the performance of our method on the five considered benchmark datasets in Tab. 2. For these experiments, we use the SwinIR backbone. Overall, due to the out-of-distribution nature of the data and the small size of some legacy datasets (e.g., 5 small images for Set5), the results are less consistent. This suggests that future work on ASSR would benefit from using larger-scale datasets in the future. Nonetheless, our methods perform best in 12 out of 15 cases. We once again observe that the performance of Thera-S is often comparable to that of methods that require

Method	Set5			Set14			B100			Urban100			Manga109		
	$\times 2$	$\times 3$	$\times 4$	$\times 2$	$\times 3$	$\times 4$	$\times 2$	$\times 3$	$\times 4$	$\times 2$	$\times 3$	$\times 4$	$\times 2$	$\times 3$	$\times 4$
MetaSR	38.26	34.77	32.47	34.14	30.66	28.85	32.39	29.31	27.75	33.29	29.12	26.76	39.46	34.62	31.37
LIIF	38.28	34.87	32.73	34.14	30.75	28.98	32.39	29.34	27.84	33.36	29.33	27.15	39.57	34.68	31.71
LTE	38.33	34.89	32.81	34.25	30.80	29.06	32.44	29.39	27.86	33.50	29.41	27.24	39.63	34.79	31.79
CUF	38.38	34.92	32.83	34.33	30.84	29.05	<u>32.47</u>	29.40	27.88	<u>33.65</u>	29.55	27.32	—	—	—
CiaoSR	38.38	34.91	32.84	34.33	30.82	29.08	<u>32.47</u>	29.42	27.90	<u>33.65</u>	29.52	27.42	39.67	34.84	31.91
CLIT	38.41	34.97	32.86	34.27	30.85	29.08	32.46	29.42	27.91	33.56	29.43	27.25	—	—	—
Thera-S	38.32	34.88	32.75	<u>34.30</u>	30.85	29.07	32.46	29.39	27.88	33.61	<u>29.56</u>	27.25	39.62	34.93	31.91
Thera-M	38.36	34.90	32.80	<u>34.30</u>	<u>30.86</u>	29.12	<u>32.47</u>	29.40	27.89	33.58	<u>29.56</u>	27.27	<u>39.70</u>	35.02	<u>32.04</u>
Thera-L	38.41	<u>34.93</u>	32.82	34.33	30.87	<u>29.11</u>	32.49	29.42	27.91	33.67	29.62	<u>27.33</u>	39.71	<u>35.01</u>	32.07

Table 2. Evaluation on common benchmark datasets for in-distribution scale factors, with a SwinIR backbone. The numbers represent PSNR in dB, calculated on the luminance (Y) channel of the YCbCr representation following previous work.

	(2, 4)	(2, 6)	(2, 12)	(2, 24)	(3, 12)	(3, 24)	(4, 24)
LIIF [11]	44.88	43.75	42.21	41.48	43.64	42.52	44.20
LTE [22]	44.10	44.40	44.37	44.40	48.33	48.48	51.42
CiaoSR [8]	44.24	43.31	42.10	41.56	41.47	41.03	45.47
Thera-S	45.79	46.67	46.80	46.89	52.38	52.66	54.84
Thera-M	45.26	46.10	46.34	46.41	51.91	52.16	54.64
Thera-L	<u>45.42</u>	<u>46.24</u>	<u>46.43</u>	<u>46.47</u>	51.56	51.77	54.33

Table 3. Comparison of multi-scale consistency (in PSNR) for various combinations of scaling factors.

orders of magnitude more parameters.

In our qualitative analysis – an excerpt of which is given in Fig. 5 – we observe that Thera achieves a more faithful and perceptually more convincing reconstruction, in particular with repeating structure. This once again highlights the advantages of using an accurate observation model in our field formulation.

4.2. Multi-scale consistency

We are interested in learning a super-resolution model that is *consistent across scales*. For instance, if we super-resolve an image with a scaling factor of $\times 4$ then downsample it by a factor of $\times 2$, we expect the result to be very similar to what we get by simply super-resolving the original image by a factor of $\times 2$. We report in Tab. 3 the quality of this match for several scaling factor pairs for Thera – which uses a formal observation model – and for three comparison methods that learn such model from data. First, we notice that better super-resolution quality does not correlate with scale consistency – *e.g.*, LTE achieves better consistency than CiaoSR for most scaling factor pairs. Second, while other methods generally exhibit good consistency, even for out of distribution (OOD) scales, our formal model is superior for all scaling factor combinations, often by a large margin, while requiring only a single parameter κ to be learned (if any, since κ can also be fixed as we show below).

4.3. Ablation studies

In Tab. 4, we ablate individual components and design choices of our method to understand their contribution to the overall performance. These comparisons are done using Thera-M using the EDSR-baseline backbone.

Single scale training. We ran three experiments using a single scale ($\times 2$, $\times 3$, $\times 4$) to test how this affects scale generalization. κ was fixed for these experiments since it requires multiscale training to be optimized. We observe equal or even superior performance compared to our base case for the scale used for training (marked in yellow in Tab. 4), but we see a significant drop in generalization.

Trainable κ . We observe a small drop in performance when using the fixed, theoretically derived value for κ (Eq. (5)). This suggests that there are still effects that have not been accounted for in our model, but the effects are very minor.

Geometric self-ensemble. As observed by previous work [24, 40, 41], we see a notable boost in performance when using geometric self-ensemble (GSE). Nevertheless, if a user prioritizes speed over quality, this addition can be disabled without retraining the network at test-time.

Total variation. We observe negligible effects for in-domain scaling factors when no TV is used, but performance degrades significantly for out-of-distribution scales.

No thermal activations. We replace thermal activations (Eq. (4)) for standard ReLU activations. What remains is only the hypernetwork controlling the parameters of the local fields. A loss in performance shows the value of our proposed thermal activation for multiscale representation.

Shared components. We observe a noticeable performance drop in all scales if we make the components \mathbf{W}_1 an output of the hypernetwork Ψ . Despite being even more flexible, it seems challenging to learn per-field components and other correlated parameters simultaneously.

4.4. Limitations and future work

Thermal activations as introduced in this paper, and by extension our proposed ASSR method, come with relatively strict architectural requirements that only allow for a single hidden layer in the neural field. While this can be beneficial from a computational standpoint, it limits hierarchical feature learning and potentially makes modeling of complex non-linear relations harder. While we have compensated for the relatively less expressive fields with a higher-capacity hypernetwork, we speculate that there may be ways to extend the signal-theoretic guarantees of Thera to multi-layer

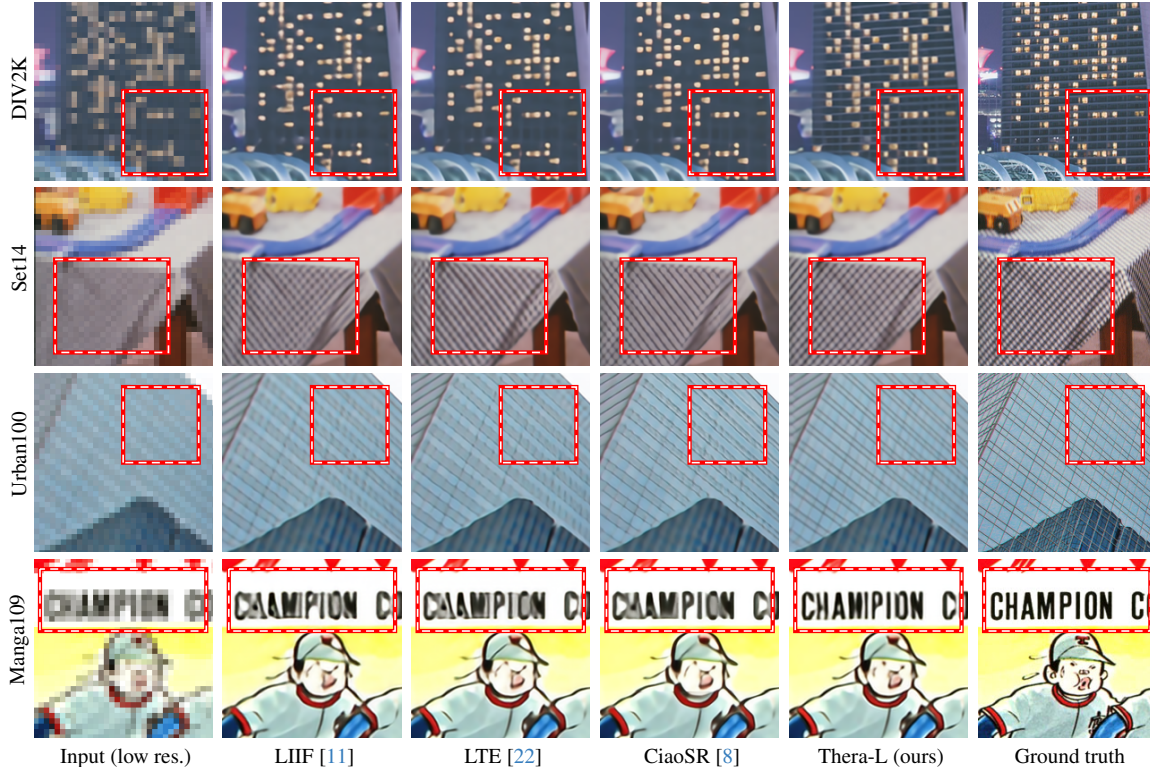


Figure 5. Qualitative examples from four datasets for $\times 6$ super-resolution. We use the SwinIR [23] backbone for all methods. More examples are given in Appendix B.

Method	In-distribution			Out-of-distribution		
	$\times 2$	$\times 3$	$\times 4$	$\times 6$	$\times 18$	$\times 30$
Thera-M	34.86	31.21	29.22	26.94	22.33	20.60
$\times 2$ only, fixed κ	34.98	30.96	28.81	26.40	21.93	20.30
$\times 3$ only, fixed κ	34.71	31.22	29.22	26.88	22.24	20.53
$\times 4$ only, fixed κ	34.44	31.14	29.22	26.95	22.30	20.58
Fixed κ	34.85	31.20	29.22	26.93	22.30	20.58
No GSE	34.79	31.14	29.16	26.88	22.28	20.56
No TV prior	34.87	31.21	29.21	26.86	20.82	19.12
No ξ	34.80	31.12	29.13	26.87	22.28	20.58
Non-shared comps.	34.80	31.13	29.14	26.87	22.28	20.57

Table 4. Ablations have been run using Thera-M using the EDSR-baseline backbone, a representative case for all other settings.

architectures in future work. This could result in higher parameter efficiency, and potentially better generalization. There may also be other formulations with similar characteristics which do not require the usage of a hypernetwork, which may allow for more streamlined training.

We noticed a relative drop in performance w.r.t. other methods for $\times 2$ SR. We speculate that our weakness relative to higher scaling factors is due to this scale being close to the interface between continuous (field) and grid (pixel) representations, which Thera’s formalism does not model. Further exploration on this transition regime for such hybrid structures would be useful to better understand and

use these hybrid representations. This could also benefit Instant-NGP [31] and related methods.

Finally, we have only explored TV as a method for regularizing Φ at $t = 0$, but we expect other signal priors to be even more effective. Priors at $t = 0$, possible only by using Thera, have the potential to regularize the continuous signal itself, and therefore improve SR performance for all scaling factors.

5. Conclusion

We have developed a novel paradigm for arbitrary-scale super-resolution by combining traditional signals theory with modern implicit neural representations. Our method, Thera, implicitly describes an image as a combination of sinusoidal components which can be modulated based on their frequency to perform Gaussian filtering (anti-aliasing) analytically with little overhead. Our experimental evaluation shows that Thera is superior to competing methods in most cases, while also being more parameter efficient and providing theoretical guarantees. We also hope to inspire others to apply Thera to other problems where it is likely to be beneficial due to its Gaussian observation model, such as demosaicing, burst super-resolution, and neural radiance fields.

References

- [1] Eirikur Agustsson and Radu Timofte. NTIRE 2017 challenge on single image super-resolution: Dataset and study. In *IEEE Conference on Computer Vision and Pattern Recognition Workshops*, 2017. 5
- [2] Jimmy Lei Ba, Jamie Ryan Kiros, and Geoffrey E Hinton. Layer normalization. *arXiv preprint arXiv:1607.06450*, 2016. 3
- [3] Jonathan T Barron, Ben Mildenhall, Matthew Tancik, Peter Hedman, Ricardo Martin-Brualla, and Pratul P Srinivasan. Mip-NeRF: A multiscale representation for anti-aliasing neural radiance fields. In *IEEE/CVF International Conference on Computer Vision*, pages 5855–5864, 2021. 1, 2
- [4] Jonathan T Barron, Ben Mildenhall, Dor Verbin, Pratul P Srinivasan, and Peter Hedman. Mip-NeRF 360: Unbounded anti-aliased neural radiance fields. In *IEEE/CVF Conference on Computer Vision and Pattern Recognition*, pages 5470–5479, 2022. 2
- [5] Jonathan T Barron, Ben Mildenhall, Dor Verbin, Pratul P Srinivasan, and Peter Hedman. Zip-NeRF: Anti-aliased grid-based neural radiance fields. *arXiv preprint arXiv:2304.06706*, 2023. 1, 2
- [6] Marco Bevilacqua, Aline Roumy, Christine Guillemot, and Marie Line Alberi-Morel. Low-complexity single-image super-resolution based on nonnegative neighbor embedding. In *British Machine Vision Conference*, 2012. 5
- [7] James Bradbury, Roy Frostig, Peter Hawkins, Matthew James Johnson, Chris Leary, Dougal Maclaurin, George Necula, Adam Paszke, Jake VanderPlas, Skye Wanderman-Milne, and Qiao Zhang. JAX: composable transformations of Python+NumPy programs, 2018. 5
- [8] Jiezhong Cao, Qin Wang, Yongqin Xian, Yawei Li, Bingbing Ni, Zhiming Pi, Kai Zhang, Yulun Zhang, Radu Timofte, and Luc Van Gool. CioSR: Continuous implicit attention-inattention network for arbitrary-scale image super-resolution. In *IEEE/CVF Conference on Computer Vision and Pattern Recognition*, pages 1796–1807, 2023. 1, 2, 3, 4, 5, 6, 7, 8
- [9] Yukang Cao, Guanying Chen, Kai Han, Wenqi Yang, and Kwan-Yee K. Wong. JIFF: Jointly-aligned implicit face function for high quality single view clothed human reconstruction. In *IEEE/CVF Conference on Computer Vision and Pattern Recognition*, pages 2729–2739, 2022. 2
- [10] Hao-Wei Chen, Yu-Syuan Xu, Min-Fong Hong, Yi-Min Tsai, Hsien-Kai Kuo, and Chun-Yi Lee. Cascaded local implicit transformer for arbitrary-scale super-resolution. In *IEEE/CVF Conference on Computer Vision and Pattern Recognition*, pages 18257–18267, 2023. 1, 2, 4, 6, 3
- [11] Yinbo Chen, Sifei Liu, and Xiaolong Wang. Learning continuous image representation with local implicit image function. In *IEEE/CVF Conference on Computer Vision and Pattern Recognition*, pages 8628–8638, 2021. 1, 2, 3, 4, 5, 6, 7, 8
- [12] Riccardo de Lutio, Stefano D’Aronco, Jan Dirk Wegner, and Konrad Schindler. Guided super-resolution as pixel-to-pixel transformation. In *IEEE/CVF International Conference on Computer Vision*, pages 8829–8837, 2019. 2
- [13] Simon Giebenhain, Tobias Kirschstein, Markos Georgopoulos, Martin Rünz, Lourdes Agapito, and Matthias Nießner. Learning neural parametric head models. In *IEEE/CVF Conference on Computer Vision and Pattern Recognition*, pages 21003–21012, 2023. 2
- [14] David Ha, Andrew M. Dai, and Quoc V. Le. HyperNetworks. In *International Conference on Learning Representations*, 2017. 2
- [15] Dan Hendrycks and Kevin Gimpel. Gaussian error linear units (gelus). *arXiv preprint arXiv:1606.08415*, 2016. 3
- [16] Wenbo Hu, Yuling Wang, Lin Ma, Bangbang Yang, Lin Gao, Xiao Liu, and Yuewen Ma. Tri-MipRF: Tri-mip representation for efficient anti-aliasing neural radiance fields. In *IEEE/CVF International Conference on Computer Vision*, pages 19774–19783, 2023. 1, 2
- [17] Xuecai Hu, Haoyuan Mu, Xiangyu Zhang, Zilei Wang, Tieniu Tan, and Jian Sun. Meta-SR: A magnification-arbitrary network for super-resolution. In *IEEE Conference on Computer Vision and Pattern Recognition*, pages 1575–1584, 2019. 1, 2, 5, 6
- [18] Jia-Bin Huang, Abhishek Singh, and Narendra Ahuja. Single image super-resolution from transformed self-exemplars. In *IEEE Conference on Computer Vision and Pattern Recognition*, pages 5197–5206, 2015. 5
- [19] Shengyu Huang, Zan Gojcic, Zian Wang, Francis Williams, Yoni Kasten, Sanja Fidler, Konrad Schindler, and Or Litany. Neural LiDAR fields for novel view synthesis. In *IEEE/CVF International Conference on Computer Vision*, 2023. 2
- [20] Tero Karras, Miika Aittala, Samuli Laine, Erik Härkönen, Janne Hellsten, Jaakko Lehtinen, and Timo Aila. Alias-free generative adversarial networks. *Advances in Neural Information Processing Systems*, 34:852–863, 2021. 2
- [21] Diederik P Kingma and Jimmy Ba. Adam: A method for stochastic optimization. In *International Conference on Learning Representations*, 2015. 5
- [22] Jaewon Lee and Kyong Hwan Jin. Local texture estimator for implicit representation function. In *IEEE/CVF Conference on Computer Vision and Pattern Recognition*, pages 1929–1938, 2022. 1, 2, 4, 5, 6, 7, 8
- [23] Jingyun Liang, Jiezhong Cao, Guolei Sun, Kai Zhang, Luc Van Gool, and Radu Timofte. SwinIR: Image restoration using Swin transformer. In *IEEE/CVF International Conference on Computer Vision*, pages 1833–1844, 2021. 6, 8, 2
- [24] Bee Lim, Sanghyun Son, Heewon Kim, Seungjun Nah, and Kyoung Mu Lee. Enhanced deep residual networks for single image super-resolution. In *IEEE Conference on Computer Vision and Pattern Recognition Workshops*, pages 136–144, 2017. 5, 6, 7
- [25] Zhuang Liu, Hanzi Mao, Chao-Yuan Wu, Christoph Feichtenhofer, Trevor Darrell, and Saining Xie. A convnet for the 2020s. In *Proceedings of the IEEE/CVF conference on computer vision and pattern recognition*, pages 11976–11986, 2022. 4, 2, 3
- [26] Ilya Loshchilov and Frank Hutter. SGDR: Stochastic gradient descent with warm restarts. *arXiv preprint arXiv:1608.03983*, 2016. 5

- [27] David Martin, Charless Fowlkes, Doron Tal, and Jitendra Malik. A database of human segmented natural images and its application to evaluating segmentation algorithms and measuring ecological statistics. In *IEEE International Conference on Computer Vision*, pages 416–423. IEEE, 2001. 5
- [28] Yusuke Matsui, Kota Ito, Yuji Aramaki, Azuma Fujimoto, Toru Ogawa, Toshihiko Yamasaki, and Kiyoharu Aizawa. Sketch-based manga retrieval using manga109 dataset. *Multimedia Tools and Applications*, 76:21811–21838, 2017. 5
- [29] Lars Mescheder, Michael Oechsle, Michael Niemeyer, Sebastian Nowozin, and Andreas Geiger. Occupancy networks: Learning 3d reconstruction in function space. In *IEEE Conference on Computer Vision and Pattern Recognition*, 2019. 1, 2
- [30] Ben Mildenhall, Pratul P Srinivasan, Matthew Tancik, Jonathan T Barron, Ravi Ramamoorthi, and Ren Ng. NeRF: Representing scenes as neural radiance fields for view synthesis. *Communications of the ACM*, 65(1):99–106, 2021. 1, 2
- [31] Thomas Müller, Alex Evans, Christoph Schied, and Alexander Keller. Instant neural graphics primitives with a multi-resolution hash encoding. *ACM Transactions on Graphics (ToG)*, 41(4):1–15, 2022. 2, 8
- [32] Alan V Oppenheim, Alan S Willsky, Syed Hamid Nawab, and Jian-Jiun Ding. *Signals and systems*. Prentice hall Upper Saddle River, NJ, 1997. 3
- [33] Jeong Joon Park, Peter Florence, Julian Straub, Richard Newcombe, and Steven Lovegrove. DeepSDF: Learning continuous signed distance functions for shape representation. In *IEEE/CVF Conference on Computer Vision and Pattern Recognition*, pages 165–174, 2019. 1, 2
- [34] Adam Paszke, Sam Gross, Francisco Massa, Adam Lerer, James Bradbury, Gregory Chanan, Trevor Killeen, Zeming Lin, Natalia Gimelshein, Luca Antiga, et al. Pytorch: An imperative style, high-performance deep learning library. *Advances in Neural Information Processing Systems*, 32, 2019. 5
- [35] Songyou Peng, Michael Niemeyer, Lars Mescheder, Marc Pollefeys, and Andreas Geiger. Convolutional occupancy networks. In *European Conference on Computer Vision*, pages 523–540. Springer, 2020. 1, 2
- [36] Leonid I Rudin, Stanley Osher, and Emad Fatemi. Nonlinear total variation based noise removal algorithms. *Physica D: nonlinear phenomena*, 60(1-4):259–268, 1992. 5
- [37] Vincent Sitzmann, Eric Chan, Richard Tucker, Noah Snavely, and Gordon Wetzstein. MetaSDF: Meta-learning signed distance functions. *Advances in Neural Information Processing Systems*, 33:10136–10147, 2020. 1, 2
- [38] Vincent Sitzmann, Julien Martel, Alexander Bergman, David Lindell, and Gordon Wetzstein. Implicit neural representations with periodic activation functions. *Advances in Neural Information Processing Systems*, 33:7462–7473, 2020. 2, 3
- [39] Matthew Tancik, Pratul Srinivasan, Ben Mildenhall, Sara Fridovich-Keil, Nithin Raghavan, Utkarsh Singhal, Ravi Ramamoorthi, Jonathan Barron, and Ren Ng. Fourier features let networks learn high frequency functions in low dimensional domains. *Advances in Neural Information Processing Systems*, 33:7537–7547, 2020. 2
- [40] Radu Timofte, Rasmus Rothe, and Luc Van Gool. Seven ways to improve example-based single image super resolution. In *IEEE Conference on Computer Vision and Pattern Recognition*, pages 1865–1873, 2016. 5, 7
- [41] Cristina N. Vasconcelos, Cengiz Oztireli, Mark Matthews, Milad Hashemi, Kevin Swersky, and Andrea Tagliasacchi. CUF: Continuous upsampling filters. In *IEEE/CVF Conference on Computer Vision and Pattern Recognition*, pages 9999–10008, 2023. 2, 4, 5, 6, 7, 3
- [42] Francis Williams, Zan Gojcic, Sameh Khamis, Denis Zorin, Joan Bruna, Sanja Fidler, and Or Litany. Neural fields as learnable kernels for 3d reconstruction. In *IEEE/CVF Conference on Computer Vision and Pattern Recognition*, pages 18500–18510, 2022. 2
- [43] Yiheng Xie, Towaki Takikawa, Shunsuke Saito, Or Litany, Shiqin Yan, Numair Khan, Federico Tombari, James Tompkin, Vincent Sitzmann, and Srinath Sridhar. Neural fields in visual computing and beyond. In *Computer Graphics Forum*, pages 641–676. Wiley Online Library, 2022. 1, 2
- [44] Yuliang Xiu, Jinlong Yang, Dimitrios Tzionas, and Michael J Black. ICON: Implicit clothed humans obtained from normals. In *IEEE/CVF Conference on Computer Vision and Pattern Recognition*, pages 13286–13296. IEEE, 2022. 2
- [45] Xingqian Xu, Zhangyang Wang, and Humphrey Shi. UltraSR: Spatial encoding is a missing key for implicit image function-based arbitrary-scale super-resolution. *arXiv preprint arXiv:2103.12716*, 2021. 2
- [46] Tarun Yenamandra, Ayush Tewari, Florian Bernard, Hans-Peter Seidel, Mohamed Elgharib, Daniel Cremers, and Christian Theobalt. i3dmm: Deep implicit 3d morphable model of human heads. In *IEEE/CVF Conference on Computer Vision and Pattern Recognition*, pages 12803–12813, 2021. 2
- [47] Roman Zeyde, Michael Elad, and Matan Protter. On single image scale-up using sparse-representations. In *International Conference on Curves and Surfaces*, pages 711–730. Springer, 2012. 5
- [48] Yulun Zhang, Yapeng Tian, Yu Kong, Bineng Zhong, and Yun Fu. Residual dense network for image super-resolution. In *IEEE Conference on Computer Vision and Pattern Recognition*, pages 2472–2481, 2018. 6
- [49] Mingwu Zheng, Hongyu Yang, Di Huang, and Liming Chen. ImFace: A nonlinear 3d morphable face model with implicit neural representations. In *IEEE/CVF Conference on Computer Vision and Pattern Recognition*, pages 20343–20352, 2022. 2

Neural Fields with Thermal Activations for Arbitrary-Scale Super-Resolution

Supplementary Material

A. Theory

A.1. Preliminaries

As was described in Sec. 3.1, the idea is to formulate a neural field $\Phi(\mathbf{x}, t)$, with \mathbf{x} being the 2-dimensional spatial coordinates (x_1, x_2) , such that Φ follows the heat equation:

$$\frac{\partial \Phi}{\partial t} = \kappa \cdot \nabla_{\mathbf{x}}^2 \Phi = \kappa \cdot \left(\frac{\partial^2 \Phi}{\partial x_1^2} + \frac{\partial^2 \Phi}{\partial x_2^2} \right). \quad (8)$$

The reason for this is that the analytical solution to the (isotropic) heat equation can be modelled as a convolution of the initial state $\Phi(\mathbf{x}, 0)$ with a Gaussian kernel

$$g(\mathbf{x}, t) = \frac{1}{4\pi\kappa t} \cdot \exp\left(-\frac{x_1^2 + x_2^2}{4\kappa t}\right). \quad (9)$$

By fitting the data at $\Phi(\mathbf{x}, 1)$, we are assuming a Gaussian point spread function (PSF) with the shape

$$\text{PSF}(\mathbf{x}) = \frac{1}{4\pi\kappa} \cdot \exp\left(-\frac{x_1^2 + x_2^2}{4\kappa}\right). \quad (10)$$

In this formulation, we attempt to recover a “pure” signal at $t = 0$ or higher sampling rates $0 < t < 1$ given an observation at $t = 1$. Note that

$$\Phi(\mathbf{x}, t) \text{ is } \begin{cases} \text{meaningless,} & \text{if } t < 0 \\ \text{pure signal,} & \text{if } t = 0 \\ \text{ill-posed,} & \text{if } 0 < t < 1 \\ I, & \text{if } t = 1 \\ \text{well-posed,} & \text{if } t > 1 \end{cases} \quad (11)$$

The ill-posed problem for $0 < t < 1$ is the interesting case. The super-resolution algorithm should somehow condition the solution space to find the appropriate solution in this domain.

For all the formulations here, we define the image I to correspond to the coordinates $x_1, x_2 \in [-0.5, 0.5]$.

A.2. Thermal diffusivity coefficient

To use the above formulations, we need to compute the thermal diffusivity coefficient κ . One way to do so is to match the cut-off frequency of the filter in Eq. (9) at $t = 1$ to the well-known Nyquist frequency given by the sampling rate. We take the cut-off frequency of the Gaussian filter defined in Eq. (9) to be the frequency whose amplitude is halved, which is

$$f_c = \sqrt{\ln(4)} \cdot \sigma_f = \frac{\sqrt{\ln(4)}}{2\pi\sqrt{2\kappa t}} \quad (12)$$

For the signal compressed into the domain $[-0.5, 0.5]$, we can compute the Nyquist frequency to be

$$f_{\text{Nyquist}} = \frac{N}{2}, \quad (13)$$

where N is the number of samples along a given dimension. This formulation assumes even sampling over x_1 and x_2 .

If we solve for $f_c = f_{\text{Nyquist}}$ at $t = 1$, we get

$$\kappa = \frac{\sqrt{\ln(4)}}{2\pi^2 N^2}. \quad (14)$$

For the Thera formulation presented in Sec. 3.2, we want Φ to contain a single pixel at $t = 1$, therefore we initialize κ with

$$\kappa = \frac{\sqrt{\ln(4)}}{2\pi^2}. \quad (15)$$

Note that the exact value of κ will depend on the exact characteristics of the system that is being modelled. Lower values of κ allow for sharper signals to be represented at any given value of t , but is also more prone to aliasing.

Finally, we would like to highlight that Eq. (12) is specific to the case where \mathbf{x} is 2-dimensional. The theoretically ideal value of κ is the only part of our formulation that does not directly apply when using fields in spaces with numbers of spatial dimensions other than 2. Nonetheless, computing κ for other cases would be a simple matter of repeating the steps above with the desired formulas for a Gaussian filter with the appropriate number of dimensions.

A.3. Relationship between t and s

Assuming that the field is learned appropriately, we still need to know at what time t we should sample from to obtain the correct (aliasing-free) signal for a different sampling rate. If we define S to be the **subsampling** rate (*i.e.*, if our base image has $N = 128$ and we want to subsample it with $N = 64$, we have $S = 2$) we need to find t such that f_{Nyquist} scales by $1/S$. Using Eq. (12) and Eq. (13), we can easily find the quadratic relationship

$$t = S^2. \quad (16)$$

For instance, if we want to upsample the image by a factor of 2, we should use

$$t = 0.5^2 = 0.25. \quad (17)$$

Thus, $0 < t < 1$ refer to super-resolution, while $t > 1$ refers to downsampling.

	In-distribution			Out-of-distribution					
	×2	×3	×4	×6	×8	×12	×18	×24	×30
LIIF [11]	.942	.883	.830	.753	.702	.641	.594	.568	.551
LTE [22]	.942	.883	.832	.755	.704	.643	.595	.569	.552
CiaoSR [8]	.942	.883	.832	.756	.706	.645	.598	.572	.551
Thera-S	.943	.884	.833	.757	.706	.644	.596	.569	.552
Thera-M	.943	.885	.834	.758	.707	.645	.596	.569	.552
Thera-L	.942	.885	.834	.759	.708	.646	.597	.570	.552

Table 5. SSIM scores (higher is better) for several methods and scaling factors evaluated on the (hold-out) DIV2K validation set. We use the SwinIR [23] backbone for all models.

Method	Set5			Set14			B100			Urban100			Manga109		
	×6	×8	×12	×6	×8	×12	×6	×8	×12	×6	×8	×12	×6	×8	×12
MetaSR	29.09	27.02	24.82	26.58	25.09	23.33	25.94	24.87	23.59	24.16	22.75	21.31	27.29	24.96	22.35
LIIF	29.46	27.36	—	26.82	25.34	—	26.07	25.01	—	24.59	23.14	—	27.69	25.28	—
LTE	29.50	27.35	—	26.86	25.42	—	26.09	25.03	—	24.62	23.17	—	27.83	25.42	—
CUF	29.57	—	—	26.91	—	—	26.11	—	—	24.69	—	—	—	—	—
CiaoSR	<u>29.62</u>	27.45	24.96	26.88	25.42	23.38	26.13	25.07	23.68	24.84	23.34	<u>21.60</u>	28.01	<u>25.61</u>	<u>22.79</u>
CLIT	29.69	27.62	—	26.94	25.55	—	26.15	25.09	—	24.77	23.33	—	—	—	—
Thera-S (ours)	29.45	27.33	25.00	26.85	25.40	23.40	26.11	25.05	23.69	24.68	23.23	21.55	27.94	25.49	22.73
Thera-M (ours)	29.47	27.43	<u>25.07</u>	26.90	25.41	<u>23.40</u>	26.13	25.07	<u>23.69</u>	24.70	23.25	21.57	<u>28.05</u>	25.59	<u>22.79</u>
Thera-L (ours)	29.48	<u>27.46</u>	25.09	26.94	<u>25.45</u>	23.42	26.14	<u>25.08</u>	23.71	<u>24.79</u>	23.32	21.62	28.13	25.69	22.85

Table 6. Evaluation on common benchmark datasets for out-of-distribution scale factors, using the SwinIR backbone. The numbers represent PSNR in dB, calculated on the luminance (Y) channel of the YCbCr representation following previous work.

A.4. Other filters

In theory, the formulation presented in Sec. 3.1 allows us to use any low-pass filter we want, since we can modulate different components freely. Gaussian filters are an obvious choice since they are often used as anti-aliasing filters and since they are fully defined by a single parameter, the standard deviation. Initial explorations of a sharp low-pass filter which completely removes components above f_{Nyquist} led to a performance reduction, likely to how this also affected gradients during training. It remains an open question whether more complex filters (*e.g.*, Butterworth filters) would improve the current formulation in any way. For quantitative evaluations this is unlikely, since the down-sampling operations use Gaussian anti-aliasing, but in real-world applications or other scenarios this may be desirable.

A.5. Initialization of components

We have noticed during our experiments that the initialization of the components (\mathbf{W}_1 in Eq. (2)) is very important. Sitzmann et al. [38] made similar observations when periodic activation functions were first used for neural fields. The final distribution of frequencies $|\nu(\mathbf{W}_1)|$ did not change much during training. Thus, we chose to initialize \mathbf{W}_1 such that

$$p(|\nu(\mathbf{w}_1)|) \propto |\nu(\mathbf{w}_1)| \quad (18)$$

up to a given maximum frequency, allotting more components to higher frequencies. See code for more details.

B. Additional qualitative results

Figure 8 and Fig. 9 contain additional qualitative results for lower and higher scaling factors, respectively. Again, we see that Thera can reconstruct the targets more faithfully. This is particularly visible in repetitive structural elements. We suspect that Thera’s inbuilt Gaussian PSF and the sinusoidal basis functions contribute to this.

C. Additional quantitative results

Table 5 contains SSIM metrics for Thera on DIV2K, which complement the PSNR values reported in Tab. 1. We observe strong performance by all Thera variants, although overall there is relatively little variance across all methods using this metric. Furthermore, Tab. 6 contains quantitative evaluations of Thera which are out of distribution both in terms of data (benchmark datasets) and in terms of scaling factors (above ×4). Finally, in Fig. 7 we show the number of additional parameters for various methods on the ×3 upsampling task.

D. Hypernetwork architecture

In Fig. 6, we show in more detail the hypernetworks used for the variants Thera-S, -M, and -L. The backbone is the same across the three variants, and extracts 64-dimensional feature maps from the input image. It is then followed by a number of (residual) ConvNeXt [25] blocks. Each block consists of *i*) a 3×3 convolution that maps to *d*-dimensional

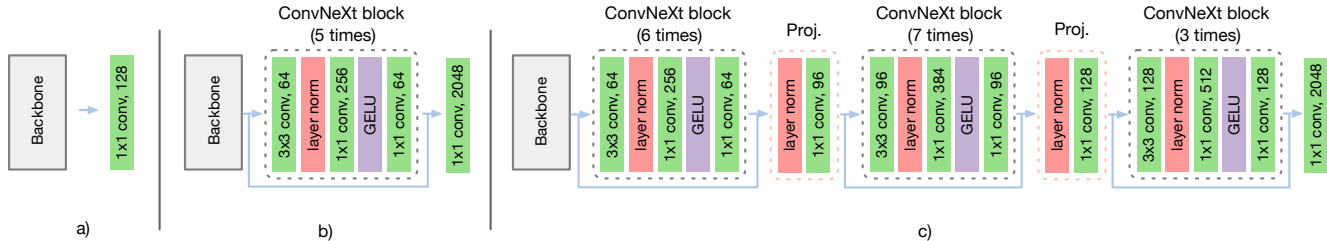


Figure 6. Schematics of the hypernetworks for a) Thera-S, b) Thera-M and c) Thera-L.

features, *ii*) a layer normalization [2] operation, *iii*) a 1×1 convolution with $4d$ filters, *iv*) a GELU [15] non-linearity, and *v*) another 1×1 convolution with d filters. Note that we decreased the kernel size of each block’s first convolution from 7×7 – as originally used by Liu et al. [25] – to 3×3 to reduce the number of parameters. Furthermore, note that in Thera-L, the first convolution per block uses d groups (effectively implementing a channel-wise convolution), while for the two smaller variants we used full convolutions, *i.e.*, a single group. In our implementation, Thera-S uses zero ConvNeXt blocks, Thera-M uses 5 blocks with $d = 64$, and Thera-L uses 6 blocks with $d = 64$ followed by 7 blocks with $d = 96$ and 3 blocks with $d = 128$. For Thera-L, we add further projection blocks between ConvNeXt blocks with different d , which consist of a layer normalization and a 1×1 convolution operation.

Finally, a 1×1 convolution maps pixel-wise features into field parameters, as done in SIREN [38]. There are 128 field parameters for Thera-S and 2048 for the larger variants Thera-M and Thera-L. Let c be the number of components used (32, 512 and 512 respectively), then we need c field parameters indicating phase shift and $3c$ field parameters for the linear mapping between components and RGB channels, resulting in a total of $4c$ field parameters produced by the hypernetwork. The total parameter count of the hypernetwork is 8,192, 0.48 M and 1.41 M for the three variants, respectively. To this we have to add the parameters of the components themselves (*i.e.*, the mapping from coordinate space to thermal activation arguments defined by \mathbf{W}_1) that are defined in a global, learnable frequency bank, adding further $2c$ parameters. We highlight that these do **not** come from the hypernetwork.

E. Replication of other methods

We encountered challenges attempting to recreate results of some of the competitor methods, which explains why some numbers are missing in various tables or differ from the originally reported ones. Details are provided below.

CUF [41]. At the time of writing, there was no public code or checkpoints available for CUF. Therefore, we could not

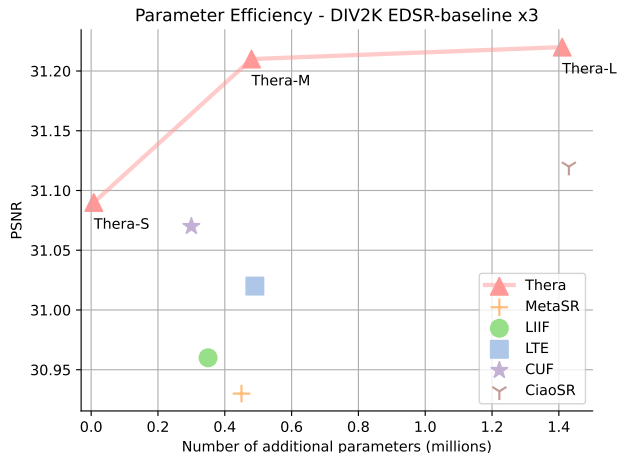


Figure 7. Plots depicting the number of additional parameters vs. PSNR on DIV2K using the EDSR-baseline backbone for the $\times 3$ upsampling task.

generate numbers for datasets and scaling factors not reported in the original paper. We have denoted those missing values with “—” in the tables. Furthermore, we could not create any qualitative samples and could not include CUF in the multi-scale consistency study in Sec. 4.2.

CLIT [10]. For CLIT, at the time of writing, there is public code available, however, checkpoints are not. We attempted to recreate their models, but due to the cascaded training schedule and the big model size, the training process would require excessive amounts of GPU hours: over 1 month using $8 \times$ Nvidia GeForce RTX 3090s. The authors did unfortunately not respond to our requests for the trained checkpoints used in their paper.

CiaoSR [8]. We noticed that CiaoSR’s border cropping prior to evaluation on the DIV2K dataset in the official implementation deviated slightly from the rest of the comparison methods. We aligned this to align the evaluation of all methods and re-computed all DIV2K numbers. This explains the slight deviation from the original paper.

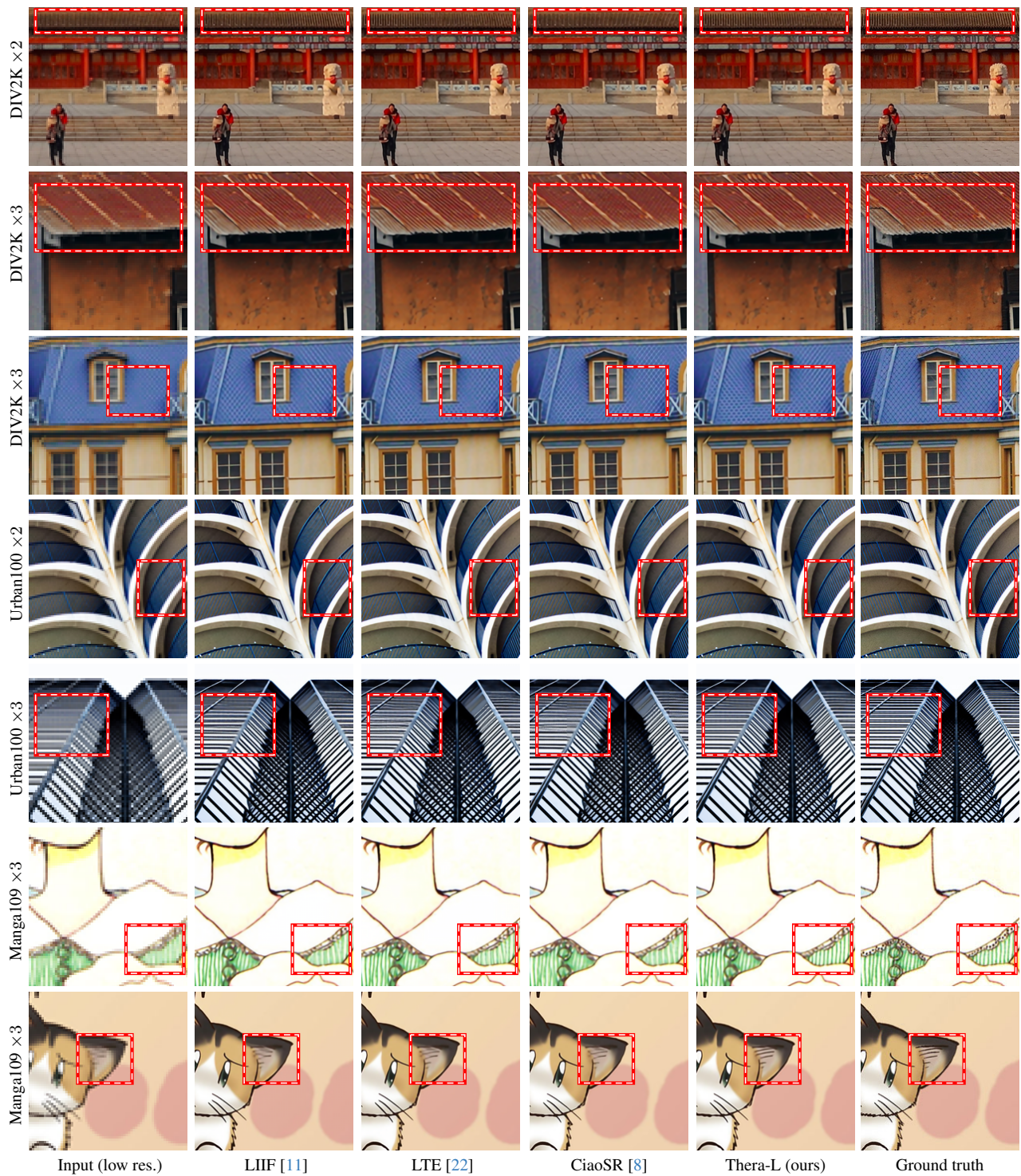


Figure 8. Further qualitative examples for $\times 2$ and $\times 3$ upsampling factors. Best viewed zoomed in.

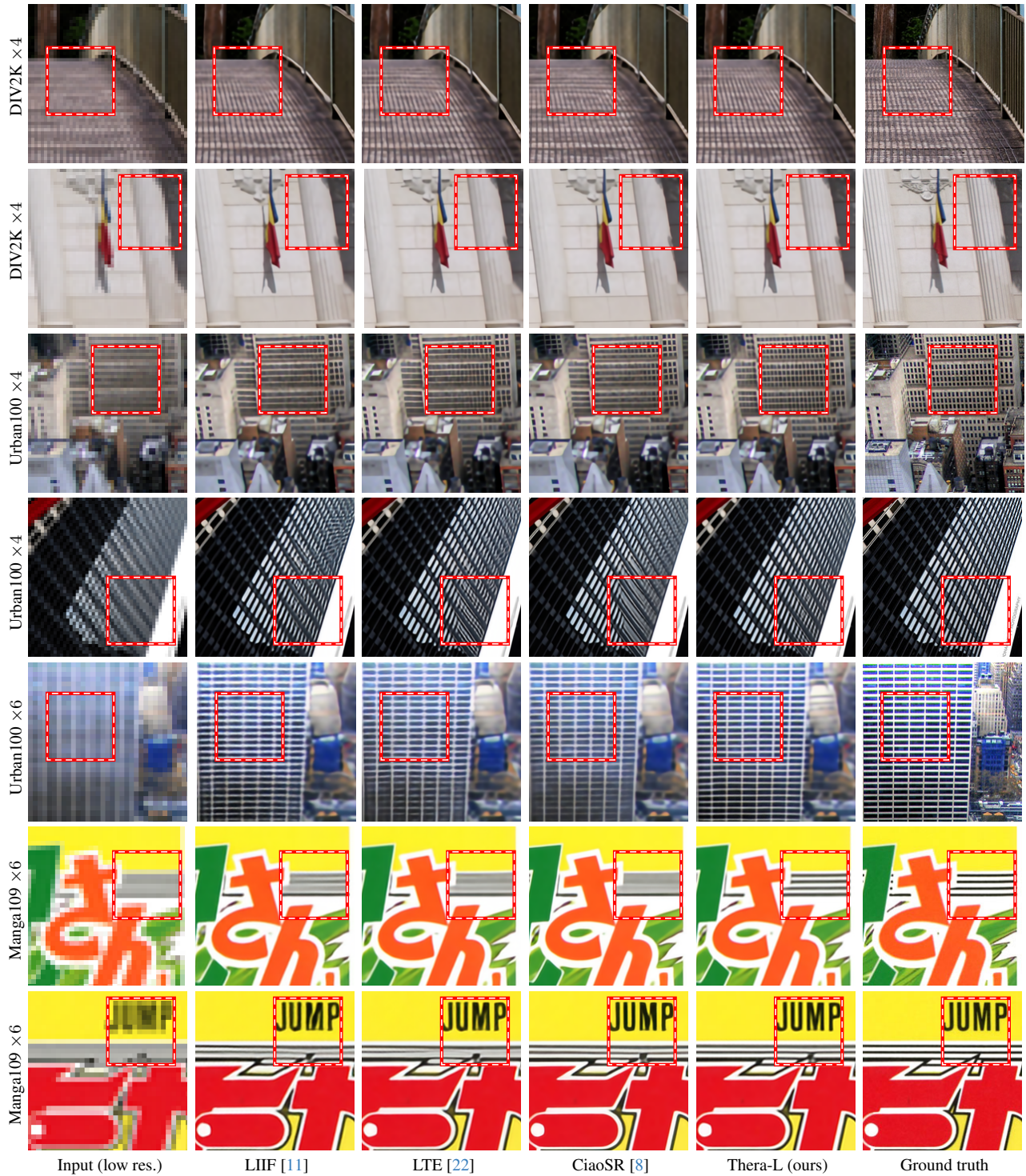


Figure 9. Further qualitative examples for $\times 4$ and $\times 6$ upsampling factors. Best viewed zoomed in.